Title
Context-dependent regulation of ferroptosis sensitivity.

Journal
Cell Chemical Biology, 29(9)

Authors
Magtanong, Leslie
Mueller, Grace
Williams, Kevin
et al.

Publication Date
2022-09-15

DOI
10.1016/j.chembiol.2022.06.004

Peer reviewed

HHS Public Access

Author manuscript

Cell Chem Biol. Author manuscript; available in PMC 2023 September 15.

Context-Dependent Regulation of Ferroptosis Sensitivity

Leslie Magtanong[1], **Grace D. Mueller**[1], **Kevin J. Williams**[2,3,4], **Maximilian Billmann**[5], **Katherine Chan**[6], **David A. Armenta**[1], **Jason Moffat**[6], **Charles Boone**[6], **Chad L. Myers**[5,7], **James A. Olzmann**[8,9], **Steven J. Bensinger**[2,4], **Scott J. Dixon**[1,*]

[1]Department of Biology, Stanford University, Stanford, CA 94305, USA

[2]Department of Microbiology, Immunology and Molecular Genetics, University of California, Los Angeles, Los Angeles, CA 90095, USA

[3]Department of Biological Chemistry, University of California, Los Angeles, Los Angeles, CA 90095, USA

[4]UCLA Lipidomics Laboratory, University of California, Los Angeles, Los Angeles, CA 90095, USA

[5]Department of Computer Science and Engineering, University of Minnesota-Twin Cities, 200 Union Street, Minneapolis, MN 55455, USA.

[6]Department of Molecular Genetics, University of Toronto, Toronto, Ontario, Canada

[7]Program in Biomedical Informatics and Computational Biology, University of Minnesota-Twin Cities, 200 Union Street, Minneapolis, MN 55455, USA.

[8]Departments of Molecular and Cell Biology and Nutritional Sciences and Toxicology, University of California, Berkeley, Berkeley, CA 94720, USA

[9]Chan Zuckerberg Biohub, San Francisco, CA 94158, USA.

SUMMARY

Ferroptosis is an important mediator of pathophysiological cell death and an emerging target for cancer therapy. Whether ferroptosis sensitivity is governed by a single regulatory mechanism is unclear. Here, based on the integration of 24 published genetic screens combined with targeted follow-up experimentation, we find that the genetic regulation of ferroptosis sensitivity is highly

*Lead contact: sjdixon@stanford.edu.

AUTHOR CONTRIBUTIONS

Conceptualization, L.M. and S.J.D.; Methodology, L.M., G.D.M., K.J.W. and J.A.O.; Investigation, L.M., G.D.M., K.J.W., M.B., K.C., and D.A.A.; Writing - Original Draft, L.M. and S.J.D.; Writing - Review and Editing, L.M., G.D.M., K.J.W., J.A.O., S.J.B., and S.J.D.; Supervision, J.M., C.B., C.M., J.A.O., S.J.B. and S.J.D.

DECLARATION OF INTERESTS

J.A.O. is a member of the scientific advisory board of Vicinitas Therapeutics. S.J.D. is a co-founder of Prothegen and a member of the scientific advisory boards for Ferro Therapeutics and Hillstream BioPharma. J.A.O. and S.J.D. hold patents related to ferroptosis.

SUPPLEMENTAL INFORMATION

Supplemental information includes four figures and three tables and can be found with this article online.

variable and context-dependent. For example, the lipid metabolic gene acyl-CoA synthetase long chain family member 4 (*ACSL4*) appears far more essential for ferroptosis triggered by direct inhibition of the lipid hydroperoxidase glutathione peroxidase 4 (GPX4) than by cysteine depletion. Despite this, distinct pro-ferroptotic stimuli converge upon a common lethal effector mechanism: accumulation of lipid peroxides at the plasma membrane. These results indicate that distinct genetic mechanisms regulate ferroptosis sensitivity, with implications for the initiation and detection of this process in vivo.

Graphical Abstract

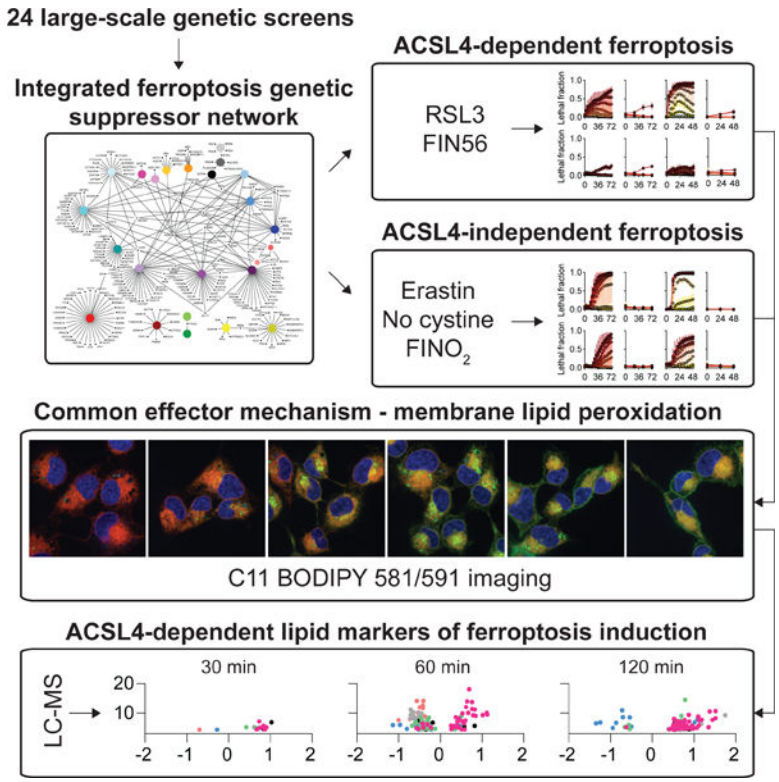

eTOC:

The genetic regulation of ferroptosis remains poorly understood. Magtanong et al demonstrate that *ACSL4*, *AGPS* and other lipid metabolic genes are context-dependent ferroptosis regulators that are not universally essential for this process. Results suggest that there may not exist a single ferroptosis genetic regulatory mechanism in all cells and conditions.

INTRODUCTION

Ferroptosis is a non-apoptotic cell death process important in pathophysiology and as a potential target for new anti-cancer therapies (Jiang et al., 2021). This process can be induced by depleting cells of the thiol-containing amino acid cysteine, direct inhibition of the glutathione-dependent lipid hydroperoxidase glutathione peroxidase 4 (GPX4), and other means (Jiang et al., 2021; Shimada et al., 2016). These stimuli allow for iron-dependent

accumulation of lipid peroxides to lethal levels (Conrad and Pratt, 2019; Wiernicki et al., 2020). Lipid peroxides form on specific polyunsaturated fatty acid (PUFA)-containing phospholipids, whose eventual destruction likely causes lethal permeabilization of the plasma membrane (Doll et al., 2017; Kagan et al., 2017; Magtanong et al., 2019). The regulation of ferroptosis sensitivity by intracellular signaling and metabolic networks remains poorly understood.

To search for conserved regulators of ferroptosis execution, we aggregated data from 24 large-scale chemical genetic screens. Unexpectedly, few genes appeared to be essential for ferroptosis execution in all contexts. Subsequent investigation established that the key PUFA lipid metabolic enzyme acyl-CoA synthetase long chain family member 4 (ACSL4) is more important for the execution of ferroptosis following direct GPX4 inactivation than cystine deprivation, while the key ether lipid synthesis enzyme alkylglycerone phosphate synthase (AGPS) is entirely dispensable for ferroptosis, at least in some contexts. This analysis reveals unanticipated diversity in the genetic regulation of ferroptosis sensitivity.

RESULTS

An integrated ferroptosis genetic suppressor network

To better understand the regulation of ferroptosis, we curated 24 published large-scale genetic loss of function screens for genes reported to promote ferroptosis execution (i.e., gene silencing or disruption inhibited cell death) (Table S1). These screens used 11 different cell line genetic backgrounds and nine different pro-ferroptotic conditions, which we reasoned would provide a sound basis to search for common regulators of this pathway. Across all 24 screens, a cumulative total of 363 non-redundant genes were reported to suppress ferroptosis, with a median of 9.5 genes identified per screen (range = 1–34) (Table S2). To investigate further, we standardized gene annotations, mapped mouse genes to human orthologs where possible, filtered out pseudogenes and non-coding RNAs, and identified instances where the same gene was identified in more than one screen. This enabled us to construct an integrated network that ultimately linked the 24 screens to 239 unique protein-coding genes (Figure 1A). Annotating this network using the database for annotation, visualization and integrated discovery (DAVID) bioinformatic resource (Huang et al., 2009), suggested significant enrichment for gene products localized to multiple intracellular compartments (cytoplasm, endoplasmic reticulum, peroxisome and mitochondria), with diverse molecular functions (kinase activity, acyltransferase activity), and involved in a range of biological processes, most notably lipid metabolism (Figure 1B-D). This analysis highlighted the potentially complex regulation of ferroptosis by spatially and functionally distinct cellular systems.

Based on the canonical model of ferroptosis regulation (Jiang et al., 2021), we initially hypothesized that our network would pinpoint many genes that were commonly essential for ferroptosis execution. Of the 24 screens examined, 16 employed methods that should in principle have enabled the function of most genes in the genome to be assayed, while eight screens were conducted using reagent libraries targeted to different gene sub-sets (Table S1). This would make it impossible to identify any gene in all 24 screens. However, to our surprise, only 24 genes were identified even two or more times, and 215 genes in the

network (90% of the total) were identified in just one of 24 screens (Table S2). The lack of concordance in our network could be explained by large numbers of false negatives and false positives in each individual screen; this possibility cannot easily be ruled out. However, an alternative possibility was that the regulation of ferroptosis sensitivity varied substantially between cell lines and lethal conditions.

To investigate further, we focused on 15 genes identified three or more times in our network. On average, these genes were more highly ranked in each screen than the 224 genes identified in less than three screens (Mann-Whitney U test, $P < 0.001$), consistent with higher confidence roles in ferroptosis regulation (Figure 1E). Indeed, among these genes, *ACSL4*, *LPCAT3*, *POR* and *KEAP1* are validated ferroptosis regulators (Dixon et al., 2015; Doll et al., 2017; Forcina et al., 2022; Sun et al., 2016; Yan et al., 2020; Zou et al., 2020b), while *GPAT4*, *CHP1*, *RETSAT* and *TXNDC17* are plausible ferroptosis regulators based on the functions of these genes in lipid metabolism and redox homeostasis (Espinosa and Arner, 2019; Pang et al., 2017; Zhu et al., 2019) (Figure 1F). Still, these 15 genes were identified on average in only 20% of all screens (median = 5/24, range 3–15) (Figure 1F). Using data available through the Dependency Map portal (depmap.org), we considered and rejected the possibility that differences in basal gene expression or gene essentiality between cell lines provided a general explanation for the lack of overlap between screens (Figure S1A,B). For example, 786-O, OVCAR8, and HT-1080 cell lines expressed similar levels of *ACSL4* and *AGPS*, yet these lipid metabolic genes were identified as being essential for ferroptosis only in genome-wide screens conducted in 786-O and OVCAR8 cells. These findings suggested that the genetic regulation of ferroptosis could vary substantially between contexts.

ACSL4 is a context-specific ferroptosis regulator

As a case study to investigate the potential context-specific regulation of ferroptosis we first focused on *ACSL4*. ACSL4 is generally considered a universal ferroptosis regulator (Jiang et al., 2021), but there is also evidence that ferroptosis can be executed in the absence of this gene in some contexts (Chu et al., 2019; Shui et al., 2021). Overall, *ACSL4* was found more often any other gene in our network (Figure 1C). Strikingly, however, *ACSL4* disruption was identified in 14/16 screens that induced ferroptosis by inhibiting GPX4 but only 1/8 of screens that induced ferroptosis by depriving cells of cystine (Figure 1A). While technical issues could explain some of these differences, we also considered the alternative possibility that ACSL4 was more important for ferroptosis induced by direct GPX4 inhibition than cystine deprivation.

To investigate, we first conducted a new genome-wide CRISPR/Cas9 screen in human HAP1 haploid cells treated with the potent system x_c^- inhibitor erastin2. Overall, 340 genes were identified as significant modulators (enhancers or suppressors) of erastin2-induced cell death (FDR $q < 0.05$) (Figure 2A) (Table S3). Disruption of genes that promote glutathione and cysteine synthesis (*GCLM, SLC7A11, CTH, CBS*), amino acid homeostasis (*ATF4*), and mechanistic target of rapamycin (mTOR) signaling (*TSC1*, *TSC2*, *NPRL2*, *DEPDC5*), all sensitized to erastin2, while disruption of *SFXN1* and *KEAP1* suppressed cell death, consistent with published findings (Conlon et al., 2021; Dixon et al., 2012; Dixon et al., 2014; Dodson et al., 2019; Soula et al., 2020). By contrast, disruption of *ACSL4* and

other lipid metabolic genes found in our network (e.g., *LPCAT3*, *AGPAT3*, *CHP1*) did not suppress erastin2-induced death in HAP1 cells (Figure 2B). Previously, we identified *ACSL4* and *LPCAT3* as essential for cell death in response to direct GPX4 inhibition in KBM7 cells (Dixon et al., 2015), from which HAP1 cells are derived, suggesting that these genes could in theory have been identified in our erastin2 screen if they were important regulators.

Next, we examined unmodified (Control) and clonal *ACSL4* gene-disrupted (i.e., knockout, KO) HT-1080^{N} fibrosarcoma and A549^{N} non-small cell lung carcinoma (NSCLC) cell lines (Magtanong et al., 2019) (Figure S2A). Using a shotgun liquid chromatography coupled to mass spectrometry (LC-MS) lipidomics method (Hsieh et al., 2021), we confirmed that *ACSL4* disruption reduced the abundance of multiple PUFA-containing triacylglycerols and phospholipid species in both cell lines, especially those containing C22:6 acyl chains (Kagan et al., 2017) (Figure S2B,C). These cell lines express nuclear-localized mKate2 protein, which allowed us to precisely quantify cell death over time using the scalable time-lapse analysis of cell death kinetics (STACK) technique (Forcina et al., 2017). In line with our genetic network analysis, *ACSL4* disruption suppressed ferroptosis induced by the GPX4 inhibitor RSL3 more potently than ferroptosis induced by the system x_c^- inhibitor erastin2 or direct cystine deprivation (Figure 2C-E, S2D). In all experiments, cell death was potently suppressed by the radical trapping antioxidant ferrostatin-1 (Fer-1), demonstrating that our lethal reagents were inducing cell death via ferroptosis (Figure 2D,E). RSL3 sensitivity was restored in HT-1080 *ACSL4*^{KO1} cells by re-expressing the long isoform of ACSL4 (Kuch et al., 2014), confirming that effects on ferroptosis were due to ACSL4 loss specifically (Figure S2E,F).

Given the unexpected nature of these results, we sought additional evidence that ACSL4 was more important for ferroptosis induced by direct GPX4 inhibition than by cystine deprivation. Using isogenic HEK 293^{N} human embryonic kidney cells that do or do not express ACSL4 (Magtanong et al., 2019), we again found that disruption of *ACSL4* more strongly reduced sensitivity to RSL3 than erastin2 (Figure S2G). Furthermore, in HT-1080^{N} and two additional cancer cell lines (H1299^{N} NSCLC and T98G^{N} glioblastoma), pretreatment for 24 h with the small molecule ACSL4 inhibitor rosiglitazone (Doll et al., 2017; Kim et al., 2001), also rendered cells more resistant to ferroptosis induced by RSL3 or the structurally distinct GPX4 inhibitor ML210 than to erastin2 (Figure 2F,G). Thus, ACSL4 appeared more important for ferroptosis in response to direct GPX4 inhibition that cystine deprivation.

We recently reported that mTOR activity promotes ferroptosis in response to cystine deprivation but not GPX4 inhibition (Conlon et al, 2021). ACSL4 may modulate mTOR activity through a lipid-dependent signaling mechanism (Orlando et al., 2015). Thus, we examined whether *ACSL4* disruption enhanced mTOR pathway activity, masking a protective effect for *ACSL4* deletion in response to cystine deprivation. Arguing against this possibility, *ACSL4* disruption in HT-1080 cells did not increase the phosphorylation of key mTOR substrates, and the ATP competitive mTOR inhibitor INK128 did not fully inhibit ferroptosis in *ACSL4*^{KO1} cells, as would be expected if increased mTOR activity was masking the protective effect of *ACSL4* disruption (Figure S3A,B). Thus, altered mTOR

signaling did not appear to explain why ACSL4 was less important for ferroptosis execution in response to cystine deprivation than direct GPX4 inhibition.

We next considered the role of ACSL4 in response to additional ferroptosis-inducing conditions. Cell death induced by the oxime-containing compound FIN56, which triggers GPX4 protein degradation (Shimada et al., 2016), was potently suppressed by *ACSL4* disruption, consistent with the requirement for ACSL4 function in ferroptosis triggered by GPX4 perturbation (Figure S3C). By contrast, ferroptosis induced by the endoperoxide-containing 1,2-dioxolane $FINO_2$, which directly promotes iron oxidation (Abrams et al., 2016; Gaschler et al., 2018), was only weakly inhibited by disruption of *ACSL4*, more like cells deprived of cystine (Figure S3D). *ACSL4* disruption did not alter sensitivity to compounds that trigger non-ferroptotic cell death, confirming that ACSL4 is not a general regulator of cell death (Figure S3E). Collectively, these results suggested that ACSL4 is a lethal context-specific regulator of ferroptosis sensitivity.

Ether lipid synthesis is not essential for ferroptosis

Analysis of our genetic network suggested that other lipid metabolism genes may, like *ACSL4*, play context-specific roles in ferroptosis regulation. In particular, we focused on *AGPS*, which encodes alkylglycerone phosphate synthase. AGPS is required for the synthesis of ether lipids, a special class of phospholipids proposed to be essential for ferroptosis execution (Zou et al., 2020a). However, *AGPS* was identified as a ferroptosis suppressor gene in only 5/24 screens catalogued in our network (Figure 1A), and was not detected in our HAP1 CRISPR screen with erastin2 (Figure 2A, Table S2). We therefore hypothesized that, like *ACSL4*, *AGPS* may play a context-specific role in ferroptosis regulation. To test this hypothesis, we generated *AGPS* gene-disrupted HT-1080^N cell lines (Figure 3A), where the abundance of numerous PUFA-containing ether lipids was substantially reduced (Figure 3A,B). Surprisingly, *AGPS* disruption had little effect on sensitivity to erastin2 or RSL3 (Figure 3C, S4A). These results were consistent with the structure of our genetic suppressor network and our HAP1 CRISPR screen, which suggested that AGPS-dependent ether lipid synthesis may play a context-specific rather than universal role in ferroptosis execution.

Notably, disruption of *AGPS* re-routed PUFA species from ether lipids into diacyl phospholipids such as PE 16:0/22:6 and PE 16:0/22:4 (Figure 3B). We hypothesized that the overall abundance of PUFAs in membrane phospholipids could be a more important determinant of ferroptosis sensitivity than the specific phospholipid class (i.e., diacyl versus ether lipid). Consistent with this possibility, pre-treatment with rosiglitazone suppressed ferroptosis to a similar extent in response to RSL3 in both HT-1080^N Control and *AGPS*$^{KO1/2}$ cell lines (Figure 3D). We intended to perform the converse experiment in our *ACSL4* gene-disrupted cell lines, using a published small molecule inhibitor of AGPS, ZINC-69435460 (termed here ‘AGPSi’, (Piano et al., 2015)). However, control experiments revealed that AGPSi alone sensitized our validated *AGPS* gene-disrupted cell lines to ferroptosis (Figure S4A,B). This suggests that AGPSi has a confounding off-target effect in connection with ferroptosis regulation and should be used with caution.

Distinct ferroptotic stimuli converge on a common effector mechanism

Ferroptosis is defined by the accumulation of lipid ROS within the cell and at the plasma membrane (Kagan et al., 2017; Magtanong et al., 2019; Torii et al., 2016). Regardless of the means of induction, ferroptosis and ferroptosis-associated lipid peroxidation can be suppressed by common inhibitors, such as the radical trapping antioxidant ferrostatin-1, suggesting that the terminal fate of ferroptotic cells must share certain commonalities (Dixon et al., 2012). To investigate whether specific lipid metabolic enzymes could influence spatial patterns of lipid ROS accumulation, we performed experiments in both HT-1080 Control and *ACSL4*^{KO1} cells. Lipid ROS accumulation was visualized using C11 BODIPY 581/591 (C11), a ratiometric probe (Magtanong et al., 2019; Pap et al., 1999). In response to erastin2, both HT-1080 Control and *ACSL4*^{KO1} cells exhibited increased C11 oxidation prior to the onset of cell death, both in perinuclear regions and at the plasma membrane (Figure 4A). These results were consistent with the viability data and suggested that *ACSL4* status does not influence ferroptosis in response to cystine deprivation.

We next examined C11 oxidation in response to direct GPX4 inhibition. In Control cells, RSL3 caused increased C11 oxidation within the cell and at the plasma membrane, much like treatment with erastin2 (Figure 4B). However, in *ACSL4*^{KO1} cells, C11 was oxidized at internal sites but not at the plasma membrane (Figure 4B). Even prolonged incubation with RSL3 of up to 8 h did not result in plasma membrane C11 oxidation in *ACSL4*^{KO1} cells, and these cells continued to proliferate over 72 h, suggesting that these cells remained functionally intact (Figure 4C, S4C). As noted, C11 oxidation in RSL3-treated *ACSL4*^{KO1} cells was observed at intracellular sites at 4 h, then faded such that by 8 h little C11 oxidation was apparent (Figure 4C). Intracellular C11 oxidation was not as prominent inside *ACSL4*^{WT} cells after 2 h GPX4 inhibitor treatment (Figure 4C). In fact, in RSL3-treated Control cells we observed bright internal C11 oxidation within 15 min and subsequent oxidation of plasma membrane C11 by 90 min (Figure 4D). Thus, C11 oxidation is initiated at the cell interior then spreads to the plasma membrane in a manner that requires ACSL4 in response to GPX4 inhibition but not cystine deprivation.

Finally, we used shotgun LC-MS to correlate the observed changes in lipid oxidation with global alterations in lipid abundance in HT-1080 Control and *ACSL4*^{KO1} cells treated with RSL3 for 30, 60 or 120 minutes. The abundance of dozens of lipids were dynamically altered by RSL3 treatment, the vast majority in an ACSL4-dependent manner including numerous PUFA-containing TAGs that were increased by 30 min, and diverse PEs that were decreased at 60 min, around the time lipid oxidation was first observed to reach the plasma membrane (Figure S4D). These complex changes define a lipidomic signature that correlates with the induction of ACSL4-dependent ferroptosis over time in response to direct GPX4 inhibition and the sequential accumulation of oxidized lipids at internal sites followed by the plasma membrane.

DISCUSSION

We find little overlap between genes identified as ferroptosis regulators in two dozen published genetic screens. New genome-wide CRISPR screening, as well as targeted gene editing, lipidomic analysis, and lipid ROS imaging suggest context-specific roles for several

genes in ferroptosis execution, most notably *ACSL4* and *AGPS*. Our results are consistent with previous evidence for context-specific ferroptosis regulatory mechanisms (Soula et al., 2020; Zille et al., 2022). Compared to other cell death mechanisms like apoptosis or necroptosis, which appear to rely on a universal set of key effectors (Green, 2019), ferroptosis may be difficult to describe as a single, unitary lethal mechanism.

Our results suggest the existence of at least two distinct modes of ferroptosis execution defined by the requirement for ACSL4. ACSL4 is more important for the induction of ferroptosis in response to direct GPX4 inhibition than cystine deprivation or treatment with the iron oxidizing agent $FINO_2$. ACSL4 is also dispensable for ferroptosis in response to p53 induction and photodynamic therapy (Chu et al., 2019; Shui et al., 2021). Thus, ACSL4-independent ferroptosis may be induced by diverse stimuli. How lethal lipid peroxidation occurs under these diverse conditions in the absence of *ACSL4* remains to be clarified. One possibility is that distinct ACSL-family enzymes contribute to the pool of lipids that are oxidized in response to cystine deprivation.

The dynamics of lipid peroxidation during ferroptosis remains largely unclear. The long isoform of ACSL4, which restores sensitivity to GPX4 inhibitors in ACSL4 mutant cell lines (Figure S2E,F), is predominantly localized to the endoplasmic reticulum (ER) (Kuch et al., 2014). ACSL4 may be necessary for the synthesis of phospholipids in the ER that are required for or themselves the target of subsequent peroxidation at the plasma membrane, at least in response to direct GPX4 inhibition. It is unclear whether lipid peroxidation spreads from internal puncta and peri-nuclear membranes to the plasma membrane, or whether internal sites are simply oxidized before lipids found on the plasma membrane. Regardless, it is remarkable that both direct GPX4 inhibition and cystine deprivation appear to converge on the peroxidation of plasma membrane lipids as a final common effector for the execution of ferroptosis.

Limitations of the study

We integrated genetic screening data obtained using diverse cell lines and lethal conditions. Technical differences between the design and execution of these screens could result in false negatives that contribute to the lack of concordant results. It is also difficult in loss of function screens to assess the role of essential genes in ferroptosis suppression, which could be better conserved than for non-essential genes. The lethal conditions and cell-based models examined here represent only a fraction of potential conditions where ferroptosis may be observed in vitro and in vivo. Our results were also obtained using cancer cell lines, and the role of ACSL4 in lipid oxidation in non-cancer cells and tissues could be different. It will be important to survey ferroptosis in more conditions to arrive at a clearer understanding of how plastic this mechanism may be in different contexts.

SIGNIFICANCE

Ferroptosis is a non-apoptotic cell death process whose genetic regulation appears to be complex. We find little overlap in the genes identified as essential for ferroptosis in two dozen published genetic screens. Detailed investigation indicates that *ACSL4* is more important for the execution of ferroptosis in response to direct GPX4 inhibition than cysteine

deprivation. An implication of these findings is that it may be misleading to use *ACSL4* dependence as a universal test for the occurrence of this lethal process. Our results also do not support a universal role for AGPS or other lipid metabolic enzymes in ferroptosis regulation. Broadly, our results indicate that it may be impossible to define a single, unitary ferroptosis regulatory pathway. These findings highlight an inherent plasticity in the genetic regulation of ferroptosis.

STAR METHODS

RESOURCE AVAILABILITY

Lead Contact—Further information and requests for resources and reagents should be directed to and will be fulfilled by the Lead Contact, Scott Dixon (sjdixon@stanford.edu).

Materials Availability—Plasmids generated in this study will be shared by the lead contact upon request.

Data and Code Availability

- Unprocessed western blot images and unprocessed lipidomics data have been deposited at Mendeley and are publicly available as of the date of publication. The DOI is listed in the key resources table. Microscopy images reported in this paper will be shared by the lead contact upon request.
- This paper does not report original code.
- Any additional information required to reanalyze the data reported in this paper is available from the lead contact upon request.

Experimental Model and Subject Details

Cell lines and culture conditions: Validated cell lines were originally obtained from primary vendors, then immediately expanded and frozen in multiple aliquots. Thawed cell lines were validated based on known morphology, growth rates, and ferroptosis sensitivity profiles. Low passage cells (< 30 passages) were used for all experiments. HT-1080 cells (gender: male; Cat# CCL-121) were obtained from ATCC (Manassas, VA). Nuclear mKate2-expressing (denoted by superscript 'N') A549^{N} (gender: male) and HT-1080^{N} were described previously (Forcina et al., 2017). HEK-293^{N} (gender: female) Control cells were described previously (Perez et al, 2020). HEK-293 *ACSL4*^{KO1} and *ACSL4*^{KO2} and HT-1080 Control, *ACSL4*^{KO1}, and *ACSL4*^{KO2}, H1299^{N} (gender: male), and T98G^{N} (gender: male) were described previously (Forcina et al., 2017; Magtanong et al., 2019; Tarangelo et al., 2018). Polyclonal populations of all non-mKate2^{+} cell lines used in this study were transduced with lentivirus directing the expression of nuclear-localized mKate2 (Cat# 4476, Essen BioSciences, Ann Arbor, MI, USA) as described previously (Forcina et al., 2017). A549^{N}, H1299^{N}, HEK-293^{N}, and T98G^{N} cells were grown in Dulbecco's modified Eagle medium (DMEM, Cat# MT-10–013-CV, Thermo Fisher Scientific, Waltham, MA), 10% fetal bovine serum (FBS, Cat# 26140–079, Gibco), and 0.5 U/mL Pen/Strep (P/S, Cat# 15070–063, Gibco). HT-1080 cells were grown in DMEM supplemented with 10% FBS, 0.5 U/mL P/S and 1x non-essential amino acids (NEAAs, Cat# 11140–050, Gibco). Minus

cystine medium was constituted using DMEM (Cat# 17–204-CI, Thermo Fisher Scientific) supplemented with 10% dialyzed FBS (Thermo Fisher Scientific, Cat#26400044), 0.5 U/mL P/S, 1x NEAAs, 201 μM L-methionine (Cat# M9625, Sigma Aldrich, St. Louis, MO) and 3.9962 μM L-glutamine (Cat# G3126, Sigma Aldrich). Hanks' Balanced Salt solution (HBSS, Cat# −134) and trypsin (Cat# 25200114) were from Gibco. 1x phosphate buffer solution (PBS, Cat# 97062–338) was from VWR (Radnor, PA). For all experiments, cells were trypsinized and counted using a Cellometer Auto T4 cell counter (Nexcelom, Lawrence, MA). Cells were grown and treated in a humidified 37°C, 5% CO_2 incubator, unless specified otherwise.

Method Details

Network construction and analysis: All relevant screens reported in PubMed (https://pubmed.ncbi.nlm.nih.gov) through the end of December 2020 were analyzed. Loss of function ferroptosis suppressor genetic screens included small interfering RNA (siRNA), short hairpin RNA (shRNA), CRISPR, and gene-trap methods (see Table S1). All genes defined as functionally significant in each respective screen by the authors' own criteria were initially included in the analysis. Network visualization was performed using Cytoscape 3.8.0 (https://cytoscape.org) (Shannon et al., 2003). For each gene included in Table S2, the gene name reported in the original screen was verified via the National Center for Biotechnology Information Gene database (https://www.ncbi.nlm.nih.gov/gene) and if necessary, updated to the current standard. NCBI gene type was used to annotate pseudogenes, ncRNAs, anti-sense RNAs, and one unknown gene, as well as pinpoint three mouse-only genes that were not included in the final network. In the network, mouse gene names are reported using the human uppercase letter convention for simplicity. The 239 protein coding genes in the network were analyzed using the DAVID bioinformatics resource with standard settings (Huang et al., 2009). The Functional_Annotations category was used to extract cellular component, molecular function, and biological processes annotations. All significant annotations are reported. A PubMed (https://pubmed.ncbi.nlm.nih.gov) search with the term "gene X AND ferroptosis" was performed on March 17, 2022, for each of the 15 genes identified three or more times, to identify the number of abstracts containing each gene in relation to ferroptosis.

Shotgun lipidomics sample treatment, preparation and analysis: The day before the experiment, cells were seeded into 10 cm dishes (Cat# CC7682–3394, USA Scientific, Ocalal, FL) as follows: 2 million A549^{N} Control, *ACSL4*^{KO1}, or *ACSL4*^{KO2} cells/plate for basal level measurements; 1 million HT-1080 Control or *ACSL4*^{KO1} cells/plate x 2 plates for each time point (0, 30, 60, 120 min) of RSL3 treatment; 900,000 HT-1080^{N} Control, *AGPS*^{KO1}, or *AGPS*^{KO2} cells/plate for basal level measurements. For all experiments, the next day, cells were harvested (for measuring basal levels) or treated for the appropriate time prior to harvesting by trypsinization. Cells were counted and then transferred using a glass Pasteur pipette to conical-bottom glass centrifuge tubes (Cat# 05–569-2, Fisher Scientific) or a 15 mL conical tube. Cells were pelleted (55 x g, 5 min, room temperature) and the supernatant was discarded. Cell pellets in glass centrifuge tubes were immediately frozen at −80°C. Cell pellets in 15 mL conical tubes were resuspended in 0.5 mL 1x PBS, transferred to a flat-bottom, open top glass tube, and immediately frozen at −80°C. Four (A549^{N}

Control and *ACSL4*$^{KO1/2}$ basal levels and HT-1080^{N} Control and *AGPS*$^{KO1/2}$ basal levels), three (A549^{N} DMSO or RSL3 and DMSO or erastin2), and three (HT-1080^{N} Control and *ACSL4*^{KO1} RSL3 time course) independent experiments treated on different days for each condition were collected for analysis. Lipids were then extracted and analyzed exactly as described (Hsieh et al., 2021).

CRISPR/Cas9 suppressor screen: A CRISPR/Cas9 screen was performed in HAP1 cells as described (Aregger et al., 2020). Briefly, 100 million HAP1 cells stably expressing Cas9 were transduced with the TKOv3 lentiviral library containing a total of 71,090 guide RNAs, at an M.O.I. of ~0.3 and then after 24 h recovery selected in puromycin (1 μg/mL) for 48 h. Cells were then split into three separate populations (Day 0), on day 4, each population was subdivided into erastin2 (1 μM) treatment or DMSO arms, and passaged every three days for a total of three treatment rounds. Cells were harvested on day 15 day, corresponding to ~17 population doublings for control-treated cell populations. Vehicle control and erastin2-treated samples were pelleted, prepared for next generation sequencing, and analyzed as described (Aregger et al., 2020). Quantitative genetic interaction (qGI) scores were computed by comparing the effects on sgRNA representation in the final pools between DMSO control and erastin2-treated conditions.

Cell death analysis using STACK: Cell death was analyzed using the scalable time-lapse analysis of cell death kinetics (STACK) technique. Cell lines stably expressing nuclear-localized mKate2 were incubated in medium with SYTOX Green (20 nM). Counts of live (mKate2^{+}) and dead (SG^{+}) objects were obtained from images acquired every 2 or 4 h on the Essen IncuCyte Zoom (Essen BioScience, Ann Arbor, MI). The following image extraction parameter values were used to count all cell lines except mKate2^{+} objects for A549^{N} *ACSL4*^{KO1} and SG^{+} objects in the ACSL4 rescue experiment: *for SG*$^{+}$ *objects*: Adaptive Threshold Adjustment 3; Edge Split On; Edge Sensitivity −7; Filter Area min 0 μm^{2} max 750 μm^{2}; *for mKate2*$^{+}$ *objects*: Adaptive Threshold Adjustment 2.5; Edge Split On; Edge Sensitivity −2; Filter Area min 50 μm^{2}, maximum 8100 μm^{2}; Eccentricity max 0.9; and *for Overlap objects*: Filter area min 50 μm^{2}, maximum 8100 μm^{2}. For mKate2^{+} objects for A549^{N} *ACSL4*^{KO1}, Adaptive Threshold Adjustment was set to 0.15. For SG^{+} objects in the ACSL4 rescue experiment, the Filter Area min was set to 40 μm^{2}. Counts were exported to Excel (Microsoft Corporation, Redmond, WA) and lethal fraction (LF) scores were computed from mKate2^{+} and SG^{+} counts as described (Forcina et al., 2017), with the additional step of removing ‘overlap’ double positive counts from live cell counts at each timepoint (Inde et al., 2020). LF scores were exported to Prism 9.0.1 (GraphPad Software, La Jolla, CA).

Cell death assays: For erastin2 and RSL3 dose response experiments, the day before the experiment, 4,000 HT-1080^{N}, 5,000 A549^{N} or 20,000 HEK-293^{N} Control and *ACSL4*$^{KO1/2}$ cells/well were seeded into a 96-well plate (Cat# 3904, Corning); for HT-1080^{N} Control and *AGPS*$^{KO1/2}$ cells, 4,000 cells/well were seeded into a 96-well plate (Cat# 3598, Corning). For the remaining lethal compound dose response experiments, the day before the experiment, 5,000 HT-1080^{N} Control and *ACSL4*$^{KO1/2}$ cells/well were seeded into a 96-well plate. The lethal compounds (and final high concentration) tested were: bortezomib

(200 nM), camptothecin (10 μM), CIL56 (20 μM), erastin2 (8 μM), FIN56 (20 μM), $FINO_2$ (20 μM), RSL3 (8 μM), staurosporine (500 nM), thapsigargin (250 nM) and vinblastine (100 nM). For all compounds, the next day, cells were treated with the appropriate treatment medium containing SYTOX Green (20 nM). Cells were imaged on the Essen IncuCyte Zoom and analyzed using STACK as described above. Three or more independent experiments treated on different days were performed for each condition.

For the cystine deprivation experiments, the day before the experiment, 10,000 HT-1080^N Control and *ACSL4*$^{KO1/2}$ cells/well were seeded into a 96-well plate (Corning). The following day, the medium was removed, and the cells were washed once with HBSS to remove traces of +cystine medium, then treated with standard HT-1080 medium or -cystine medium. Both culture media contained SYTOX Green (20 nM), and then cells were imaged on the Essen IncuCyte Zoom and analyzed using STACK as described above. Three independent experiments treated on different days were performed for each condition.

For pre-treatment experiments, the day before the pre-treatment, cells were seeded as follows: HT-1080^N Control and *ACSL4*$^{KO1/2}$, H1299^N, or T98G^N: 500 cells/well into a 384-well plate (Corning); HT-1080^N Control and *AGPS*$^{KO1/2}$ cells: 2,000 cells/well into a 96-well plate (Corning). For all cell lines, the next day, the cell culture medium was replaced with medium containing the appropriate combination of DMSO (vehicle), rosiglitazone (25 μM), and AGPSi (500 μM). 24 h later, the medium was replaced with the appropriate lethal compound treatment (note that all pre-treatment conditions were maintained during the lethal compound treatments). For all experiments, SYTOX Green (20 nM) was included in the treatment medium. Cells were imaged on the Essen IncuCyte Zoom and analyzed using STACK as described above. Three or more independent experiments treated on different days were performed for each condition.

ACSL4 rescue experiments: The day before the transfection, HT-1080^N *ACSL4*^{KO1} cells were seeded at 90,000 or 180,000 cells/well into 12-well (for cell death analysis) or 6-well (for western blot analysis) plates (Cat# 3513/6, Corning), respectively. The following day, cells were transfected using Lipofectamine LTX with Plus Reagent (Cat# 15338100, ThermoFisher) according to the manufacturer's protocol. Cells were transfected with plasmids directing the expression of S-tagged *ACSL4* short or long isoforms. The short isoform of *ACSL4* was PCR amplified from pDONR221-*ACSL4* (Harvard PlasmID Database, clone HsCD00042852) and ligated into the NheI and KpnI sites of the pcDNA3.1(−) S-tag plasmid (Christianson et al., 2011). The long isoform of *ACSL4* was PCR amplified from the pSin-EF2-*ACSL4*-HA (a kind gift from Hua Xiao) and ligated into the BamHI and KpnI sites of the pcDNA3.1(−) S-tag plasmid. 1 (cell death) or 2 (western blot analysis) μg of plasmid DNA (*ACSL4*^{short}*-S-tag* or *ACSL4*^{long}*-S-tag*) or water (mock) was used for transfection. The transfection mix was left on the cells for 6 hours, removed, and replaced with fresh medium. For cell death analysis, the next day the cells were treated ± RSL3 (1 μM) ± ferrostatin-1 (1 μM). SYTOX Green (20 nM) was included in the lethal treatment mixture. The cells were imaged on the Essen IncuCyte Zoom and analyzed using STACK as described above. Three or more independent experiments treated on different days were performed for each condition. For western blot analysis, the next day the cells were placed on ice, washed once with cold 1x PBS, and then harvested by scraping. The

cells were pelleted (500 x g, 5 min, room temperature), and the cell pellets were frozen at −80 °C until needed.

CRISPR/Cas9 genome editing and DNA sequencing: Gene-disrupted A549^{N} cells were generated using *ACSL4* single-guide RNA (sgRNA) primers 5'-CACCGGTAGTGGACTCACTGCACT-3' and 5'-AAACAGTGCAGTGAGTCCACTACC-3' that were described previously (Magtanong et al., 2019). Gene-disrupted HT-1080^{N} cells were generated using sgRNAs designed with CHOP CHOP (https://chopchop.cbu.uib.no). The primer sequences used were as follows: AGPS_sg1_F: 5'-CACCGTGGGTATCTACTCGCGCATC-3'; AGPS_sg1_R: 5'-AAACGATGCGCGAGTAGATACCCAC-3'. sgRNA-containing plasmids were cloned using the same protocol described previously (Magtanong et al., 2019). Once monoclonal cell lines were established, genomic DNA from candidate knockout clones was isolated using the NucleoSpin Tissue kit (Cat# 740952, Takara Bio USA Inc, Mountain View, CA). DNA amplicons were generated using the following primers: ACSL4_conf_F1: 5'-ACCCCCAAACTCCAACTCTT-3', ACSL4_conf_R1: 5'-GGGACCAGGGAAATCCTAAG-3' (Magtanong et al, 2019), AGPS_sg1_conf_F1: 5'-TGGCCTTAAAACAAAAGGATGT-3', AGPS_sg1_conf_R1: 5'-TTTGAGACAGAATCTCGCTCTG-3'. Amplicons were purified using a QIAGEN PCR Purification column (Cat# 28106, QIAGEN) and sent for sequencing using the following primers: ACSL4_seq: 5'-TAAAATGGCTAAACAACACC-3' (Magtanong et al, 2019), AGPS_sg1_seq: 5'-CAAAGTGCTGGGATTACAG-3'. Sequence alignments to determine insertions/deletions were performed using TIDE (Brinkman et al., 2014). A549^{N} *ACSL4*^{KO1} has a 22 bp deletion and *ACSL4*^{KO2} has a 13 bp deletion. HT-1080^{N} *AGPS*^{KO1} (sg1) has a 4 bp deletion and *AGPS*^{KO2} (sg1) has a 1 bp deletion. All deletions result in premature stop codons just downstream of the respective cut sites.

Western blot analysis: For INK128-treated cells, four days before treatment, 10,000 HT-1080^{N} Control or 20,000 HT-1080^{N} *ACSL4*^{KO1} cells/well were seeded into 6-well plates (Corning). After four days, cells were treated ± INK128 (1 μM). After 24 h, the cells were harvested by trypsinization, pelleted (55 x g, 5 min, room temperature), washed once with 1x PBS, then spun down again (55 x g, 5 min, room temperature). The cell pellets were then immediately stored at −80 °C until needed. For A549^{N} Control, *ACSL4*^{KO1}, and *ACSL4*^{KO2} cell lines and for HT-1080^{N} *AGPS* Control, *AGPS*^{KO1}, and *AGPS*^{KO2} cell lines, at the time of cell collection for gDNA extraction and sequencing, cells (~2–3 million) were also collected for protein extraction and western blot analysis. The cells were collected by trypsinization. The pellet was spun down (55 x g, 5 min, room temperature), washed once with 1x PBS, then spun down again (55 x g, 5 min, room temperature). The cell pellets were then immediately stored at −80 °C until needed.

For all cell pellets, on the day of cell lysis, the pellets were thawed on ice and immediately lysed with 75–100 μL of RIPA/SDS + 1:200 Protease Inhibitor Cocktail (Cat# P8340, Sigma-Aldrich) + 5 mM NaF (for ± INK128 conditions only; Cat# S6776, Sigma-Aldrich). Lysates were sonicated [(1 s on, 1 s off, 60 % amplitude) x 10 cycles] and then centrifuged (18,000 x g, 15 min, 4 °C). Lysates were quantified using a Pierce BCA assay kit (Cat#

23225, Thermo Scientific) with a standard BSA curve. Equal amounts of protein were combined with 4x Bolt LDS Sample Buffer (Cat# B0007) and 10x Bolt Sample Reducing Agent (Cat# B0009) (Life Technologies), then loaded onto a Bolt 4–12% Bis-Tris Plus Gel (Cat# NW04120BOX; Life Technologies). Protein was transferred to a nitrocellulose membrane using an iBlot2 transfer stack (Cat# IB23001, Life Technologies). The membrane was blocked using Intercept Blocking Buffer (Cat# 927–60001, LI-COR Biotechnology, Lincoln, NE) (1 h, room temperature) and then incubated in the appropriate primary antibody mixture (1.5 h, room temperature or 4 °C, overnight). Primary antibodies used were α-ACSL4 (Cat# 22401–1-AP, Proteintech, Rosemont, IL; 1:2,000 dilution), α-AGPS (Cat# 21011–1-AP, Proteintech; 1:1,000 dilution), α-phospho-4E-BP1 (Thr37/46, Cat# 2855T; 1:1,000 dilution, Cell Signaling Technology, Danvers, MA), α−4E-BP1 (Cat# 9644S, Cell Signaling Technology; 1:1,000 dilution), α-GAPDH (Cat# 2118, Cell Signaling Technology; 1:1,000 dilution), α-phospho-RSP6 (Ser235/236, Cat# 4858, Cell Signaling Technology; 1:1,000 dilution), α-RPS6 (Cat# 2217, Cell Signaling Technology; 1:1,000 dilution), and α-alpha-tubulin (Cat# MS581P1, Millipore Sigma, Billerica, MA; 1:4,000 dilution). The primary antibody buffer was Intercept (LI-COR). The membrane was then washed in 1x TBST (5 min, room temperature, three times) and incubated in secondary antibody mixture (1 h, room temperature). Secondary antibodies (LI-COR; 1:15,000 dilution) used were 680LT donkey α-mouse (Cat# 926–68022), 680LT donkey α-rabbit (Cat# 926–68023), 800CW donkey-anti-mouse (Cat# 926–32212), and 800CW donkey α-rabbit (Cat# 925–32213). The secondary antibody buffer was Intercept (LI-COR) or 1:1 TBST:Intercept. The membrane was washed 1x TBST (5 min, room temperature, three times) and then scanned on an Odyssey CLx Imaging System (LI-COR). When necessary, membranes were stripped with 1x Nitro Stripping Buffer (Cat# 928–40030, LI-COR; 15 min, room temperature), washed three times with 1x PBS (75–100 mL), then blocked in Intercept (LI-COR; 1 h, room temperature) prior to incubation with primary antibody. Two or more independent experiments were performed on different days for each condition.

C11 BODIPY 581/591 imaging: The day before the experiment, 150,000–175,000 HT-1080 Control or *ACSL4*^{KO1} cells/well were seeded into 6-well plates (Corning) with one 22 mm^2 no. 1.5 glass coverslip in each well. The next day, the cells were treated in as described in HT-1080 growth medium for the indicated times. After the treatment, the medium was removed, and the cells were labeled with C11 BODIPY 581/591 (5 μM) and Hoechst (1 μg/mL) dissolved in HBSS. After a 10 min incubation (37°C, 5% CO_2), the C11 BODIPY 581/591+Hoechst mixture was removed, and fresh HBSS was applied to the cells. The cover slips were removed and mounted in 25 μL HBSS onto glass microscope slides. Cells were imaged using a Zeiss Axio Observer microscope with a confocal spinning-disk head (Yokogawa, Tokyo, Japan), PlanApoChromat 63x/1.4 NA oil immersion objective, and a Cascade II:512 electron-multiplying (EM) CCD camera (Photometrics, Tucson, AZ). Images were processed in ImageJ 1.52q (Schneider et al., 2012). Imaging was performed on two or more independent experiments treated on different days for each condition.

Quantification and statistical analysis—Lethal fraction scoring was performed using Microsoft Excel 16.45 (Microsoft). Confocal images were processed in ImageJ 1.52q (U.S. National Institutes of Health, Bethesda, MD). Graphing and statistical analyses were

performed using Prism 9.0.1 (GraphPad). Statistical test details are found in the main text and figure legends.

Additional resources

Chemicals and reagents: Erastin2 was synthesized by Acme Bioscience (Palo Alto, CA). RSL3 (Cat# S8155) and INK128 (Cat# S2811) were from Selleck Chemicals (Houston, TX). SYTOX Green (Cat# S7020) was from Life Technologies. Dimethyl sulfoxide (DMSO; Cat# 276855), ferrostatin-1 (Cat# SML0583), ML210 (Cat# SML0521), methanol (Cat# 34860), rosiglitazone (Cat# R2408), staurosporine (Cat# S6942), thapsigargin (Cat# T9033), and vinblastine (Cat# V1377) were from Sigma-Aldrich (St. Louis, MO). Bortezomib (Cat# NC0587961) and camptothecin (Cat# AC276721000) were from Fisher Scientific. ZINC-69435460 (AGPSi; Cat# Z1030248250) was from Enamine US Inc. (Cincinnati, OH). C11 BODIPY 581/591 (Cat# D3861) and Hoechst (Cat# H1399) were from Molecular Probes (Eugene, OR). $FINO_2$ was a gift from Keith Woerpel (New York University, NY, NY). CIL56 and FIN56 were gifts from Rachid Skouta (UMass Amherst, Amherst, MA). C11 BODIPY 581/591 was dissolved in anhydrous methanol, and all other chemicals were dissolved in DMSO. All chemicals were stored at −20°C until use.

Supplementary Material

Refer to Web version on PubMed Central for supplementary material.

ACKNOWLEDGEMENTS

We thank T. Stearns, K. Aulakh, R. Clime, A. Habsid, A. Tong, and M. Costanzo for help with experiments, and K. Woerpel, R. Skouta, and H. Xiao for reagents. M.B. and C.L.M. were partially supported by the National Science Foundation (1818293). J.M. and C.B. were supported by a Genome Canada DIG Phase 2 award. J.M. is a Canada Research Chair Tier 2 in Functional Genomics of Cancer and C.B. holds a Canada Research Chair Tier 1 in Functional Genomics and Proteomics, is a fellow of the Canadian Institute for Advanced Research (CIFAR), and was supported by the Canadian Institutes of Health Research (PJT-180285). This work was also supported by awards from the National Institutes of Health to C.L.M. (R01HG005084, R01HG005853), J.A.O. (R01GM112948), S.J.B. (HL146358), and S.J.D. (R01GM122923).

REFERENCES

Abrams RP, Carroll WL, and Woerpel KA (2016). Five-Membered Ring Peroxide Selectively Initiates Ferroptosis in Cancer Cells. ACS Chem Biol 11, 1305–1312. [PubMed: 26797166]

Aregger M, Lawson KA, Billmann M, Costanzo M, Tong AHY, Chan K, Rahman M, Brown KR, Ross C, Usaj M, et al. (2020). Systematic mapping of genetic interactions for de novo fatty acid synthesis identifies C12orf49 as a regulator of lipid metabolism. Nat Metab 2, 499–513. [PubMed: 32694731]

Brinkman EK, Chen T, Amendola M, and van Steensel B (2014). Easy quantitative assessment of genome editing by sequence trace decomposition. Nucleic Acids Res 42, e168. [PubMed: 25300484]

Christianson JC, Olzmann JA, Shaler TA, Sowa ME, Bennett EJ, Richter CM, Tyler RE, Greenblatt EJ, Harper JW, and Kopito RR (2011). Defining human ERAD networks through an integrative mapping strategy. Nat Cell Biol 14, 93–105. [PubMed: 22119785]

Chu B, Kon N, Chen D, Li T, Liu T, Jiang L, Song S, Tavana O, and Gu W (2019). ALOX12 is required for p53-mediated tumour suppression through a distinct ferroptosis pathway. Nat Cell Biol 21, 579–591. [PubMed: 30962574]

Conlon M, Poltorack CD, Forcina GC, Armenta DA, Mallais M, Perez MA, Wells A, Kahanu A, Magtanong L, Watts JL, et al. (2021). A compendium of kinetic modulatory profiles identifies ferroptosis regulators. Nat Chem Biol

Conrad M, and Pratt DA (2019). The chemical basis of ferroptosis. Nat Chem Biol 15, 1137–1147. [PubMed: 31740834]

Dixon SJ, Lemberg KM, Lamprecht MR, Skouta R, Zaitsev EM, Gleason CE, Patel DN, Bauer AJ, Cantley AM, Yang WS, et al. (2012). Ferroptosis: an iron-dependent form of nonapoptotic cell death. Cell 149, 1060–1072. [PubMed: 22632970]

Dixon SJ, Patel DN, Welsch M, Skouta R, Lee ED, Hayano M, Thomas AG, Gleason CE, Tatonetti NP, Slusher BS, et al. (2014). Pharmacological inhibition of cystine-glutamate exchange induces endoplasmic reticulum stress and ferroptosis. Elife 3, e02523. [PubMed: 24844246]

Dixon SJ, Winter GE, Musavi LS, Lee ED, Snijder B, Rebsamen M, Superti-Furga G, and Stockwell BR (2015). Human Haploid Cell Genetics Reveals Roles for Lipid Metabolism Genes in Nonapoptotic Cell Death. ACS Chem Biol 10, 1604–1609. [PubMed: 25965523]

Dodson M, Castro-Portuguez R, and Zhang DD (2019). NRF2 plays a critical role in mitigating lipid peroxidation and ferroptosis. Redox Biol 23, 101107. [PubMed: 30692038]

Doll S, Proneth B, Tyurina YY, Panzilius E, Kobayashi S, Ingold I, Irmler M, Beckers J, Aichler M, Walch A, et al. (2017). ACSL4 dictates ferroptosis sensitivity by shaping cellular lipid composition. Nat Chem Biol 13, 91–98. [PubMed: 27842070]

Espinosa B, and Arner ESJ (2019). Thioredoxin-related protein of 14 kDa as a modulator of redox signalling pathways. Br J Pharmacol 176, 544–553. [PubMed: 30129655]

Forcina GC, Conlon M, Wells A, Cao JY, and Dixon SJ (2017). Systematic Quantification of Population Cell Death Kinetics in Mammalian Cells. Cell Syst 4, 600–610 e606. [PubMed: 28601558]

Forcina GC, Pope L, Murray M, Dong W, Abu-Remaileh M, Bertozzi CR, and Dixon SJ (2022). Ferroptosis regulation by the NGLY1/NFE2L1 pathway. Proc Natl Acad Sci U S A 119, e2118646119. [PubMed: 35271393]

Gaschler MM, Andia AA, Liu H, Csuka JM, Hurlocker B, Vaiana CA, Heindel DW, Zuckerman DS, Bos PH, Reznik E, et al. (2018). FINO2 initiates ferroptosis through GPX4 inactivation and iron oxidation. Nat Chem Biol 14, 507–515. [PubMed: 29610484]

Green DR (2019). The Coming Decade of Cell Death Research: Five Riddles. Cell 177, 1094–1107. [PubMed: 31100266]

Hsieh WY, Williams KJ, Su B, and Bensinger SJ (2021). Profiling of mouse macrophage lipidome using direct infusion shotgun mass spectrometry. STAR Protoc 2, 100235. [PubMed: 33364623]

Huang DW, Sherman BT, and Lempicki RA (2009). Systematic and integrative analysis of large gene lists using DAVID bioinformatics resources. Nat Protoc 4, 44–57. [PubMed: 19131956]

Inde Z, Forcina GC, Denton K, and Dixon SJ (2020). Kinetic Heterogeneity of Cancer Cell Fractional Killing. Cell Rep 32, 107845. [PubMed: 32640215]

Jiang X, Stockwell BR, and Conrad M (2021). Ferroptosis: mechanisms, biology and role in disease. Nat Rev Mol Cell Biol

Kagan VE, Mao G, Qu F, Angeli JP, Doll S, Croix CS, Dar HH, Liu B, Tyurin VA, Ritov VB, et al. (2017). Oxidized arachidonic and adrenic PEs navigate cells to ferroptosis. Nat Chem Biol 13, 81–90. [PubMed: 27842066]

Kim JH, Lewin TM, and Coleman RA (2001). Expression and characterization of recombinant rat Acyl-CoA synthetases 1, 4, and 5. Selective inhibition by triacsin C and thiazolidinediones. J Biol Chem 276, 24667–24673. [PubMed: 11319222]

Kuch EM, Vellaramkalayil R, Zhang I, Lehnen D, Brugger B, Sreemmel W, Ehehalt R, Poppelreuther M, and Fullekrug J (2014). Differentially localized acyl-CoA synthetase 4 isoenzymes mediate the metabolic channeling of fatty acids towards phosphatidylinositol. Biochim Biophys Acta 1841, 227–239. [PubMed: 24201376]

Magtanong L, Ko PJ, To M, Cao JY, Forcina GC, Tarangelo A, Ward CC, Cho K, Patti GJ, Nomura DK, et al. (2019). Exogenous Monounsaturated Fatty Acids Promote a Ferroptosis-Resistant Cell State. Cell Chem Biol 26, 420–432 e429. [PubMed: 30686757]

Orlando UD, Castillo AF, Dattilo MA, Solano AR, Maloberti PM, and Podesta EJ (2015). Acyl-CoA synthetase-4, a new regulator of mTOR and a potential therapeutic target for enhanced estrogen receptor function in receptor-positive and -negative breast cancer. Oncotarget 6, 42632–42650. [PubMed: 26536660]

Pang XY, Wang S, Jurczak MJ, Shulman GI, and Moise AR (2017). Retinol saturase modulates lipid metabolism and the production of reactive oxygen species. Arch Biochem Biophys 633, 93–102. [PubMed: 28927883]

Pap EH, Drummen GP, Winter VJ, Kooij TW, Rijken P, Wirtz KW, Op den Kamp JA, Hage WJ, and Post JA (1999). Ratio-fluorescence microscopy of lipid oxidation in living cells using C11-BODIPY(581/591). FEBS Lett 453, 278–282. [PubMed: 10405160]

Piano V, Benjamin DI, Valente S, Nenci S, Marrocco B, Mai A, Aliverti A, Nomura DK, and Mattevi A (2015). Discovery of Inhibitors for the Ether Lipid-Generating Enzyme AGPS as Anti-Cancer Agents. ACS Chem Biol 10, 2589–2597. [PubMed: 26322624]

Schneider CA, Rasband WS, and Eliceiri KW (2012). NIH Image to ImageJ: 25 years of image analysis. Nat Methods 9, 671–675. [PubMed: 22930834]

Shannon P, Markiel A, Ozier O, Baliga NS, Wang JT, Ramage D, Amin N, Schwikowski B, and Ideker T (2003). Cytoscape: a software environment for integrated models of biomolecular interaction networks. Genome Res 13, 2498–2504. [PubMed: 14597658]

Shimada K, Skouta R, Kaplan A, Yang WS, Hayano M, Dixon SJ, Brown LM, Valenzuela CA, Wolpaw AJ, and Stockwell BR (2016). Global survey of cell death mechanisms reveals metabolic regulation of ferroptosis. Nat Chem Biol 12, 497–503. [PubMed: 27159577]

Shui S, Zhao Z, Wang H, Conrad M, and Liu G (2021). Non-enzymatic lipid peroxidation initiated by photodynamic therapy drives a distinct ferroptosis-like cell death pathway. Redox Biol 45, 102056. [PubMed: 34229160]

Soula M, Weber RA, Zilka O, Alwaseem H, La K, Yen F, Molina H, Garcia-Bermudez J, Pratt DA, and Birsoy K (2020). Metabolic determinants of cancer cell sensitivity to canonical ferroptosis inducers. Nat Chem Biol 16, 1351–1360. [PubMed: 32778843]

Sun X, Ou Z, Chen R, Niu X, Chen D, Kang R, and Tang D (2016). Activation of the p62-Keap1-NRF2 pathway protects against ferroptosis in hepatocellular carcinoma cells. Hepatology 63, 173–184. [PubMed: 26403645]

Tarangelo A, Magtanong L, Bieging-Rolett KT, Li Y, Ye J, Attardi LD, and Dixon SJ (2018). p53 Suppresses Metabolic Stress-Induced Ferroptosis in Cancer Cells. Cell Rep 22, 569–575. [PubMed: 29346757]

Torii S, Shintoku R, Kubota C, Yaegashi M, Torii R, Sasaki M, Suzuki T, Mori M, Yoshimoto Y, Takeuchi T, et al. (2016). An essential role for functional lysosomes in ferroptosis of cancer cells. Biochem J 473, 769–777. [PubMed: 26759376]

Wiernicki B, Dubois H, Tyurina YY, Hassannia B, Bayir H, Kagan VE, Vandenabeele P, Wullaert A, and Vanden Berghe T (2020). Excessive phospholipid peroxidation distinguishes ferroptosis from other cell death modes including pyroptosis. Cell Death Dis 11, 922. [PubMed: 33110056]

Yan B, Ai Y, Sun Q, Ma Y, Cao Y, Wang J, Zhang Z, and Wang X (2020). Membrane Damage during Ferroptosis Is Caused by Oxidation of Phospholipids Catalyzed by the Oxidoreductases POR and CYB5R1. Mol Cell

Zhu XG, Nicholson Puthenveedu S, Shen Y, La K, Ozlu C, Wang T, Klompstra D, Gultekin Y, Chi J, Fidelin J, et al. (2019). CHP1 Regulates Compartmentalized Glycerolipid Synthesis by Activating GPAT4. Mol Cell 74, 45–58 e47. [PubMed: 30846317]

Zille M, Oses-Prieto JA, Savage SR, Karuppagounder SS, Chen Y, Kumar A, Morris JH, Scheidt KA, Burlingame AL, and Ratan RR (2022). Hemin-Induced Death Models Hemorrhagic Stroke and Is a Variant of Classical Neuronal Ferroptosis. J Neurosci 42, 2065–2079. [PubMed: 34987108]

Zou Y, Henry WS, Ricq EL, Graham ET, Phadnis VV, Maretich P, Paradkar S, Boehnke N, Deik AA, Reinhardt F, et al. (2020a). Plasticity of ether lipids promotes ferroptosis susceptibility and evasion. Nature 585, 603–608. [PubMed: 32939090]

Zou Y, Li H, Graham ET, Deik AA, Eaton JK, Wang W, Sandoval-Gomez G, Clish CB, Doench JG, and Schreiber SL (2020b). Cytochrome P450 oxidoreductase contributes to phospholipid peroxidation in ferroptosis. Nat Chem Biol 16, 302–309. [PubMed: 32080622]

Highlights:

- An integrated genetic network reveals high variability in ferroptosis regulation
- *ACSL4* is most important for ferroptosis in response to direct GPX4 inhibition
- *AGPS* is not required for ferroptosis in all contexts
- Ferroptotic stimuli converge on plasma membrane lipid peroxidation

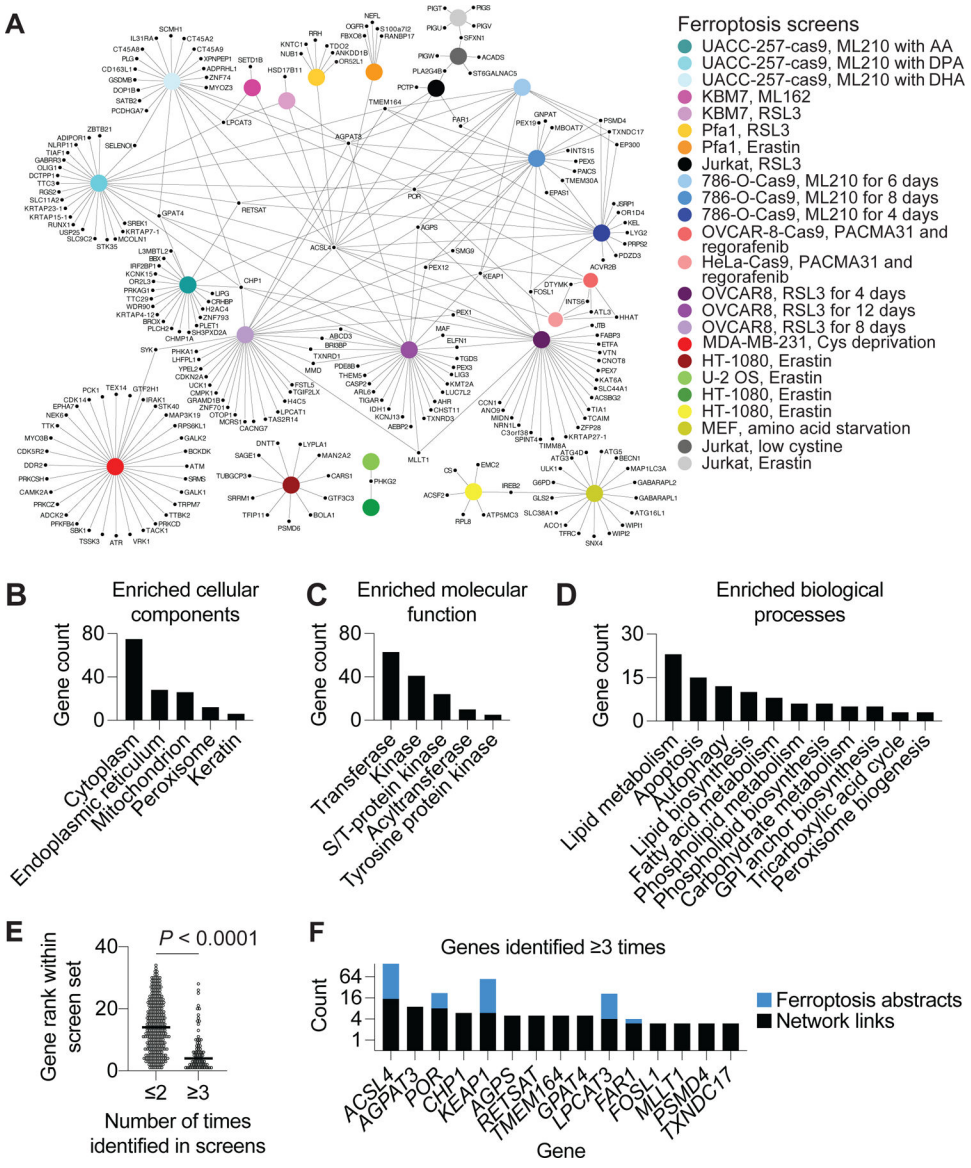

Figure 1. A literature-curated regulatory genetic network of ferroptosis suppressors.

(**A**) A consensus ferroptosis regulatory network integrating results from 24 loss of function genetic suppressor screens. Each genetic screen is indicated by a large, uniquely colored circular node that corresponds to the cell line and ferroptosis inducing condition employed. Each gene is represented by a small black node. Edges connect individual screens to specific genes.

(**B-D**) Network gene characterization using the database for annotation, visualization and integrated discovery (DAVID) bioinformatic resource.

(E) Aggregate reported gene ranks for genes identified in ≤2 or ≥3 conditions in the consensus network in **A**. Values closer to zero indicate the gene was a stronger hit.

(F) Number of times a given gene was identified in the network in **A**, overlayed with number of abstracts reported in PubMed that mention the gene name and ferroptosis together.

See also Figure S1 and Tables S1,2.

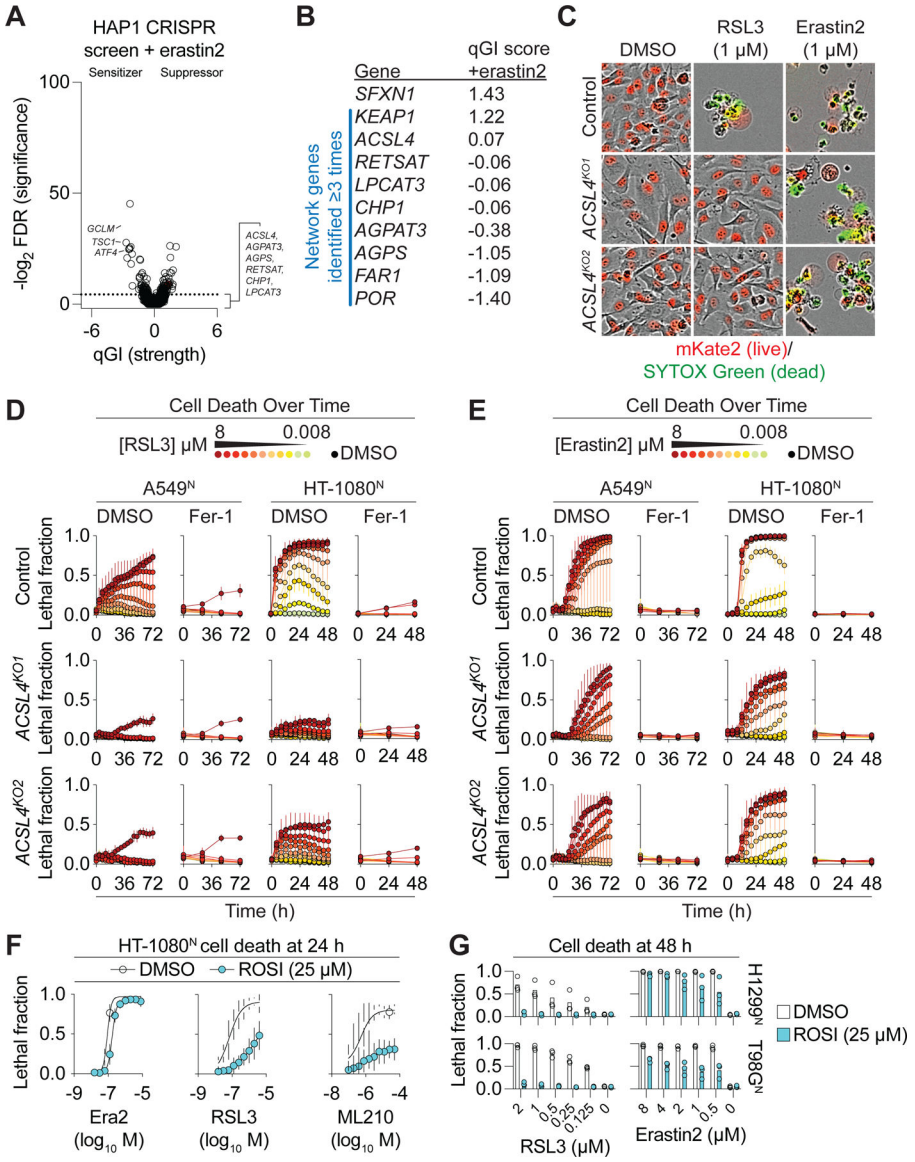

Figure 2. ACSL4 is required for ferroptosis in response to GPX4 inhibitors.

(A) Results of a HAP1 CRISPR screen. Individual genes (n = 17,800) are plotted as circles. Select sensitizer genes are indicated. qGI: quantitative genetic interaction. Horizontal dotted line: FDR $q < 0.05$.

(B) Select gene qGI scores from **A**.

(C) HT-1080^{N} cells imaged after 48 h treatment. Scale bar = 50 μm. Ct: Control. Representative of three experiments.

(**D,E**) Lethal fraction dose response curves over time for (D) RSL3- or (E) erastin2-treated cells. For lethal fraction, 0 = all cells alive, 1 = all cells dead.

(**F**,**G**) Lethal fraction of cells pre-treated for 24 h ± rosiglitazone (ROSI) prior to lethal compound treatment.

Data in (D-F) are mean ± SD of three independent experiments. Each data point in (G) is from one independent experiment. See also Figures S2,3 and Table S3.

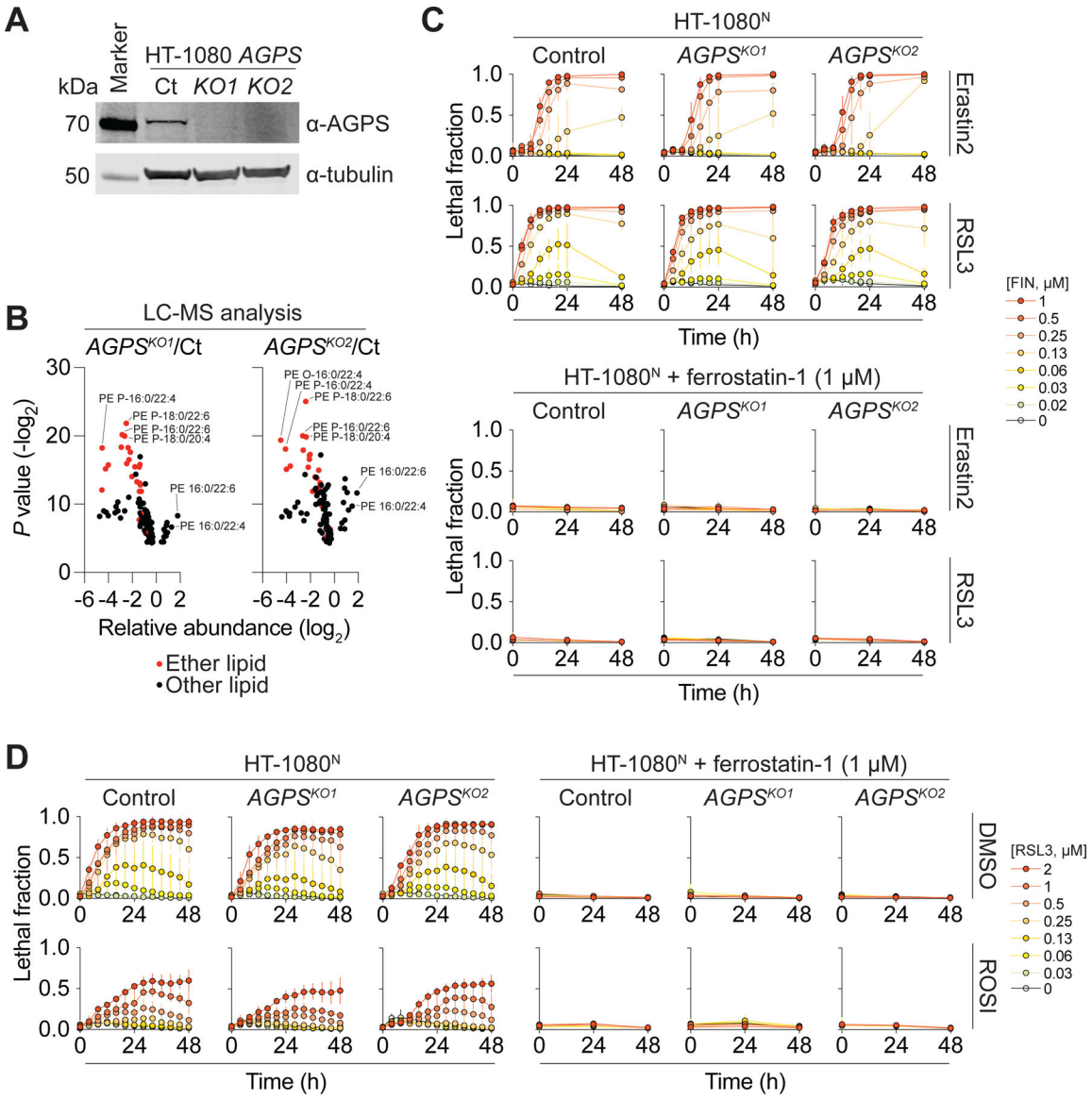

Figure 3. Ether lipids are dispensable for ferroptosis induction.

(A) Protein expression in Control (Ct) and gene-disrupted (*KO*) cell lines.

(B) Relative lipid abundance in HT-1080^{N} Control versus *AGPS*$^{KO1/2}$ cells for significantly altered lipids ($P < 0.05$, Students t-test). PE: phosphatidylethanolamine, O: ether-linked, P: vinyl ether-linked.

(**C**). Lethal fraction dose response curves over time. FIN: ferroptosis inducer.

(**D**) Lethal fraction dose response curves over time of cells pre-treated for 24 h ± rosiglitazone (ROSI, 25 μM) prior to lethal compound treatment.

Data in (B) are mean of four independent experiments. Data in (C,D) are mean ± SD from three independent experiments. See also Figure S4.

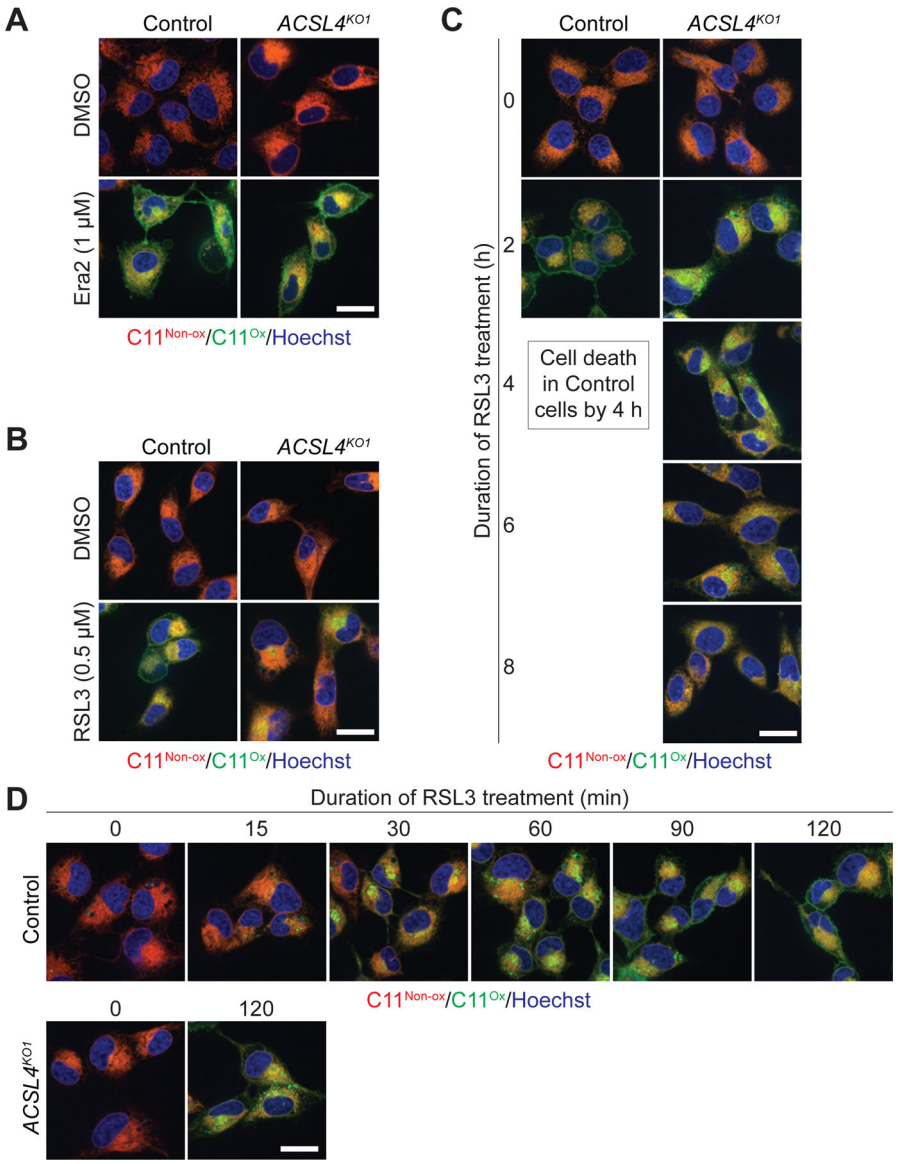

Figure 4. Context-dependent role for ACSL4 in lipid peroxidation spreading during ferroptosis.

(**A**) HT-1080 Control and *ACSL4*^{KO1} cells ± erastin2 (1 μM) for 10 h (Control) or 13 h (*ACSL4*^{KO1}). C11: C11 BODIPY 581/591, Non-ox: non-oxidized, Ox: oxidized. Scale bar = 20 μm.

(**B-D**) HT-1080 Control and *ACSL4*^{KO1} cells ± RSL3 (0.5 μM) for 2 h (B) or the indicated time points (C,D) prior to labeling with C11 and Hoechst.

For (A-D), two or more independent experiments were performed, and representative images from one experiment are shown. See also Figure S4.

KEY RESOURCES TABLE

REAGENT or RESOURCE	SOURCE	IDENTIFIER
Antibodies		
4E-BP1	Cell Signaling Technology	Cat# 9644; RRID:AB_2097841
GAPDH	Cell Signaling Technology	Cat# 2118; RRID:AB_561053
Phospho-4EB-P1 (Thr37/46)	Cell Signaling Technology	Cat# 9459; RRID:AB_330985
Phospho-RPS6 (Ser235/236)	Cell Signaling Technology	Cat# 4858; RRID:AB_916156
RPS6	Cell Signaling Technology	Cat# 2217; RRID:AB_331355
Alpha-tubulin, clone DM1A	Fisher Scientific	Cat# MS581P1
680LT Donkey-anti-mouse	LI-COR	Cat# 926–68022; RRID:AB_10715072
680LT Donkey-anti-rabbit	LI-COR	Cat# 926–68023; RRID:AB_10706167
800CW Donkey-anti-mouse	LI-COR	Cat# 926–32212; RRID:AB_621847
800CW Donkey-anti-rabbit	LI-COR	Cat# 926–32213; RRID:AB_621848
ACSL4	Proteintech	Cat# 22401–1-AP; RRID:AB_2832995
AGPS	Proteintech	Cat# 21011–1-AP; RRID:AB_2878789
Chemicals, Peptides, and Recombinant Proteins		
$FINO_2$	Abrams et al, 2016	N/A
Erastin2 (Compound 35MEW28 in Dixon et al, 2014)	Dixon et al, 2014	N/A
ZINC-69435460	Enamine	Cat# Z1030248250
Bortezomib	Fisher Scientific	Cat# NC0587961; CAS: 179324–69-7
Camptothecin	Fisher Scientific	Cat# AC276721000; CAS: 7689–03-4
C11 BODIPY 581/591 (4,4-difluoro-5-(4-phenyl-1,3-butadienyl)-4-bora-3a,4a-diaza-s-indacene-3-undecanoic acid	Molecular Probes	Cat# D3861
Hoechst	Molecular Probes	Cat# H1399
SYTOX Green	Molecular Probes	Cat# S7020
RSL3	Selleck Chemical	Cat# S8155; CAS: 1219810–16-8
Vinblastine	Selleck Chemical	Cat# S1248; CAS: 143–67-9
CIL56	Shimada et al, 2016	N/A
FIN56	Shimada et al, 2016	N/A
Chloroform	Sigma-Aldrich	Cat# 366927; CAS: 67–66-3
Dimethyl Sulfoxide (DMSO)	Sigma-Aldrich	Cat# 276855; CAS: 67–68-5
Ferrostatin-1	Sigma-Aldrich	Cat# SML0583; CAS: 347174–05-4
Methanol	Sigma-Aldrich	Cat# 34860; CAS: 67–56-1

REAGENT or RESOURCE	SOURCE	IDENTIFIER
ML210	Sigma-Aldrich	Cat# SML0521; CAS: 1360705–96-9
Rosiglitazone	Sigma-Aldrich	Cat# R2408; CAS:122320–73-4
Staurosporine	Sigma-Aldrich	Cat# S6942; CAS: 62996–74-1
Thapsigargin	Sigma-Aldrich	Cat# T9033; CAS: 67526–95-8
Deposited Data		
Unprocessed western blot images and unprocessed lipidomics data	Dixon, Scott (2022), “Context-Dependent Regulation of Ferroptosis Sensitivity”, Mendeley Data	DOI: 10.17632/fy6c7j78hp.1
Experimental Models: Cell Lines		
Human: HT-1080	ATCC	Cat# CCL-121; RRID:CVCL_0317
Human: A549^{N}	Forcina et al, 2017	N/A
Human: HT-1080^{N}	Forcina et al, 2017	N/A
Human: T98G^{N}	Forcina et al, 2017	N/A
Human: HT-1080 *ACSL4*^{KO1}	Magtanong et al, 2019	N/A
Human: H1299^{N}	Tarangelo et al, 2018	N/A
Human: A549^{N} *ACSL4*^{KO1}	This study	N/A

REAGENT or RESOURCE	SOURCE	IDENTIFIER
Human: A549^{N} *ACSL4*^{KO2}	This study	N/A
Human: HEK 293^{N}	This study	N/A
Human: HEK-293^{N} *ACSL4*^{KO1}	This study	N/A
Human: HEK-293^{N} *ACSL4*^{KO2}	This study	N/A
Human: HT-1080^{N} *ACSL4*^{KO1}	This study	N/A
Human: HT-1080^{N} *ACSL4*^{KO2}	This study	N/A
Human: HT-1080^{N} *AGPS*^{Control}	This study	N/A
Human: HT-1080^{N} *AGPS*^{KO1}	This study	N/A
Human: HT-1080^{N} *AGPS*^{KO2}	This study	N/A
Experimental Models: Organisms/Strains		
N/A		
Oligonucleotides		
ACSL4_sg2_F: CACCGGTAGTGGACTCACTGCACT	Magtanong et al, 2019	N/A
ACSL4_sg2_R: AAACAGTGCAGTGAGTCCACTACC	Magtanong et al, 2019	N/A
ACSL4_sg2_conf_F1: ACCCCCAAACTCCAACTCTT	Magtanong et al, 2019	N/A
ACSL4_sg2_conf_R1: GGGACCAGGGAAATCCTAAG	Magtanong et al, 2019	N/A
ACSL4_sg2_seq: TAAAATGGCTAAACAACACC	Magtanong et al, 2019	N/A
AGPS_sg1_F: CACCGTGGGTATCTACTCGCGCATC	This study	N/A
AGPS_sg1_R: AAACGATGCGCGAGTAGATACCCAC	This study	N/A
AGPS_sg1_conf_F1: TGGCCTTAAAACAAAAGGATGT	This study	N/A
AGPS_sg1_conf_R1: TTTGAGACAGAATCTCGCTCTG	This study	N/A
AGPS_sg1_seq: CAAAGTGCTGGGATTACAG	This study	N/A
Recombinant DNA		
IncuCyte NucLight Red Lentivirus Reagent (EF-1 α, Puro)	Essen BioScience	Cat# 4625

REAGENT or RESOURCE	SOURCE	IDENTIFIER
ACSL4-short-S-tag	This study	N/A
ACSL4-long-S-tag	This study	N/A
Software and Algorithms		
Cancer Dependency Map		https://depmap.org/portal/
National Center for Biotechnology Information Gene Database		https://www.ncbi.nlm.nih.gov/gene
PubMed		https://pubmed.ncbi.nlm.nih.gov
GraphPad Prism 9.0.1	GraphPad Software, Inc.	https://www.graphpad.com/
Database for Annotation, Visualization and Integrated Discovery (DAVID)	Huang et al, 2009	https://david.ncifcrf.gov/home.jsp
Microsoft Excel 16.45	Microsoft Corporation	N/A
ImageJ 1.52q	Schneider et al, 2012	https://imagej.nih.gov/ij
Cytoscape 3.8.0	Shannon P et al, 2003	https://cytoscape.org
Other		
N/A		